

Photoacoustic Image Reconstruction Beyond Supervised to Compensate Limit-view and Remove Artifacts

Hengrong Lan, Changchun Yang, Feng Gao, and Fei Gao*, Member, IEEE

Abstract—Photoacoustic computed tomography (PACT) reconstructs the initial pressure distribution from raw PA signals. Standard reconstruction always induces artifacts using limited-view signals, which are influenced by limited angle coverage of transducers, finite bandwidth, and uncertain heterogeneous biological tissue. Recently, supervised deep learning has been used to overcome limited-view problem that requires ground-truth. However, even full-view sampling still induces artifacts that cannot be used to train the model. It causes a dilemma that we could not acquire perfect ground-truth in practice. To reduce the dependence on the quality of ground-truth, in this paper, for the first time, we propose a beyond supervised reconstruction framework (BSR-Net) based on deep learning to compensate the limited-view issue by feeding limited-view position-wise data. A quarter position-wise data is fed into model and outputs a group full-view data. Specifically, our method introduces a residual structure, which generates beyond supervised reconstruction result, whose artifacts are drastically reduced in the output compared to ground-truth. Moreover, two novel losses are designed to restrain the artifacts. The numerical and *in-vivo* results have demonstrated the performance of our method to reconstruct the full-view image without artifacts.

Index Terms—Photoacoustic tomography, deep learning, reconstruction, convolutional neural network.

I. INTRODUCTION

As a hybrid imaging modality, photoacoustic tomography (PAT) has emerged to visualize the chromophores in biological tissue by converting absorbed optical energy into acoustic energy. It has high spatial resolution at deep penetration in tissues. Many potential applications have been explored in biomedical imaging areas, such as blood oxygen saturation (sO_2) quantification for cancer diagnostics.

This paragraph of the first footnote will contain the date on which you submitted your paper for review. It will also contain support information, including sponsor and financial support acknowledgment. This research was funded by Natural Science Foundation of Shanghai (18ZR1425000), and National Natural Science Foundation of China (61805139).

Hengrong Lan and Changchun Yang contributed equally to this work.

Hengrong Lan is with the Hybrid Imaging System Laboratory, Shanghai Engineering Research Center of Intelligent Vision and Imaging, School of Information Science and Technology, ShanghaiTech University, Shanghai 201210, China, with Chinese Academy of Sciences, Shanghai Institute of Microsystem and Information Technology, Shanghai 200050, China, and also with University of Chinese Academy of Sciences, Beijing 100049, China (e-mail: lanhr@shanghaitech.edu.cn).

Changchun Yang is with the Hybrid Imaging System Laboratory, Shanghai Engineering Research Center of Intelligent Vision and Imaging, School of Information Science and Technology, ShanghaiTech University, Shanghai 201210, China (e-mail: yangchch@shanghaitech.edu.cn).

Feng Gao is with the Hybrid Imaging System Laboratory, Shanghai Engineering Research Center of Intelligent Vision and Imaging, School of Information Science and Technology, ShanghaiTech University, Shanghai 201210, China. (gaofeng@shanghaitech.edu.cn)

Fei Gao is with the Hybrid Imaging System Laboratory, Shanghai Engineering Research Center of Intelligent Vision and Imaging, School of Information Science and Technology, ShanghaiTech University, Shanghai 201210, China (*e-mail: gaofei@shanghaitech.edu.cn).

Photoacoustic computed tomography (PACT) possesses high temporal resolution by reconstructing a photoacoustic (PA) image with single shot pulsed laser light, and provides potential preclinical and clinical prospects in thyroid cancer, breast cancer diagnostics and small animal whole body imaging [1-4]. Standard reconstruction algorithm, e.g. delay-and-sum (DAS), is widely used to rebuild PA image with high frame rate. However, ill-posed conditions, e.g. limited-view and limited elements, could cause poor quality with blurry image and artifacts. Many studies have improved the reconstruction methods to address these issues to some extent [5-9]. These methods improved the quality of PA image paid by increasing the computational complexity of reconstruction.

Recently, a new scheme, deep learning (DL), has emerged to reconstruct the PA image [10-14]. Specially, convolutional neural networks (CNN) has been a great success in computer vision area. DL enables PAT reconstruction in both image and signal domains. In signal domain, DL framework is used to denoise, enhance the number of PA signals and recover the bandwidth of PA signals [15, 16]. Then, a higher quality image can be rebuilt by standard reconstructed method. Also, DL directly learns the map from PA signals to PA image, which could contain a complex physical procedure [17-19]. However, DL has difficulty in leaning the process from signal to image for complex objects, which is susceptible to noise interference for PA signal. On the other hand, DL removes artifacts and compensates information in image domain via extracting the feature of the target [20-22]. In addition, DL inspires iterative reconstruction methods to simplify the adjustment and repeating optimization for the inverse problem by learning the regularization and some parts of the optimization procedure [23-26]. Some details of raw data could be lost during image reconstruction, e.g. superposition in DAS. Some frameworks

extract different features by combined signal and image instead of single domain. In [27, 28], the authors proposed a multi-input reconstruction framework by combining signal and image inputs. Steven Guan et al. used pixel-wise delayed data as input of CNN, which include more positional information [29]. Meanwhile, MinWoo Kim et al. converted raw data into a 3-D array, where additional positional information is considered [30]. Most works use the full-view results as ground-truth to resolve the limited-view problem, and these results of supervised learning are hardly superior over the ground-truth, which is identified as the criterion of learning outcome. However, ground-truth also contains some artifacts even though it comes from a full-view acquisition.

To go beyond crude supervision and inspired by the data of input, in this paper, we propose beyond supervised reconstruction network (BSR-Net) to compensate the limited view and remove the artifacts. A quarter position-wise delayed raw data (32-channels) is fed into model and generates delayed data of another 3 quarters positions. The ground-truth come from DAS with full-view data.

We enhance the reconstructed results by designing special supervision and ground-truth. Two different tasks are realized in a model so that beyond supervision is achieved.

The numerical experiments are demonstrated to compare the standard reconstruction (ground-truth) with proposed BSR-Net. Moreover, we perform abdomen of mice imaging experiments *in-vivo* to illustrate the superiority of our method.

Our contributions can be summarized as follows:

- We firstly introduce a DL solution to resolve the limited-view problem in PACT by feeding a quarter position-wise data.
- A universal residual structure is used to weaken the background in PA image layer by layer.
- Superior supervision is introduced that two novel losses are designed to mitigate the effect of artifacts.
- We propose a novel PA image reconstruction model, Beyond Supervised Reconstruction Network (BSR-Net), to compensate the limited view and remove the artifacts.
- We validate our method on synthetic and *in-vivo* dataset.
- Finally, we share and release the code of our model and the mice dataset, using which other researchers can reproduce and train their DL model.

II. BACKGROUNDS

A. Photoacoustic Tomography

In PAT, the initial pressure is excited by single short laser pulse, which can be expressed as [3]:

$$p_0 = \Gamma_0 \eta_{th} \mu_a F, \quad (1)$$

where Γ_0 is the Gruneisen coefficient, η_{th} is the conversion efficiency from light to heat, μ_a is the optical absorption coefficient, and F is the optical fluence. Then, the induced pressure propagates through the medium as a PA wave. The propagation can be described by the following PA equation:

$$\left(\nabla^2 - \frac{1}{v_s^2} \frac{\partial^2}{\partial t^2} \right) p(\mathbf{r}, t) = -\frac{\beta}{C_p} \frac{\partial H(\mathbf{r}, t)}{\partial t}, \quad (2)$$

where $p(\mathbf{r}, t)$ is the spatiotemporal pressure wave, v_s is the speed of sound, H denotes the heating function, β denotes the thermal coefficient of volume expansion, and C_p denotes the specific heat capacity at constant pressure. To compute PA pressure in any heterogeneous medium, we solve this equation with Green function [3]:

$$p(\mathbf{r}, t) = \frac{1}{4\pi v_s^2} \frac{\partial}{\partial t} \left[\frac{1}{v_s t} \int d\mathbf{r}' p_0(\mathbf{r}') \delta(t - \frac{|\mathbf{r} - \mathbf{r}'|}{v_s}) \right], \quad (3)$$

where $p_0(\mathbf{r}')$ is the initial pressure at detection position \mathbf{r}' . The forward operation can be modeled as a linear operator, which contains Eq. (3) and the impulse response of the transducer.

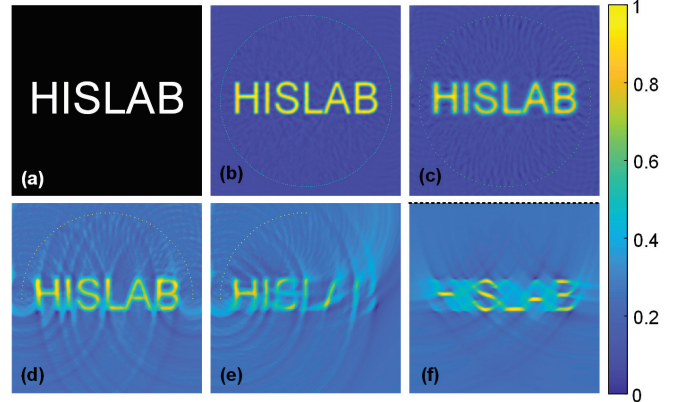


Fig. 1. Simulation results of different limited-view situations. (a) The example object. (b) reconstructed result with 256 enclosed sensors. (c) reconstructed result with 128 enclosed sensors. (d) reconstructed result with 64 half-view sensors. (e) reconstructed result with 32 quarter-view sensors. (f) reconstructed result with 128 line sensors.

B. PA Image Formation

The light uniformly illuminates the whole target in PACT, which excites the PA signals simultaneously. The transducer array is used to receive the PA data at different positions. In general, the transducer with a large detection angle is desirable in order to receive PA signals from different directions. Several algorithms are used for PA image reconstruction, within which DAS and universal back-projection (UPB) are widely used due to less computational cost and easy implementation. The UPB has the following formula:

$$p_0(\mathbf{r}) = \frac{1}{\Omega_0} \int_{S_0} \left[2p(\mathbf{r}_0, t) - \frac{2t \partial p(\mathbf{r}_0, t)}{\partial t} \right] \frac{\cos \theta_0}{|\mathbf{r} - \mathbf{r}_0|^2} dS_0, \quad (4)$$

where θ_0 is the angle between the vector pointing to the reconstruction point \mathbf{r} and transducer surface S_0 . $p(\mathbf{r}_0, t)$ is the direct back-projection of the detected PA signals, also named DAS. The assumption that the medium is acoustically lossless

and homogeneous is the common precondition of DAS and UPB.

C. The Problem of Limited-view and Artifacts in PACT

An accurate reconstruction could be maintained if the transducer encloses the target and the number of elements has enough spatial density. In fact, the transducer often only accesses the PA signals from partial coverage of the tissue due to geometric restrictions. The ill-posed situation could be caused by incomplete enclosed-angle or sparse elements, which degrades image quality or lose important information. Here, we simulated different enclosed view and spatial density of transducer in Fig. 1 [31]. A full circular transducer with enough elements (256) produces a superior result as shown in Fig. 1(b). Fig. 1(c) shows that some minor artifacts will be generated if the sensors' number decreases from 256 to 128. Once the enclosed view decreases to half view, more and more artifacts are emerged, and target is becoming blurry as Fig. 1(d) shows. A severe situation could happen if we further decrease the angle as shown in Fig. 1(e). Only the part of object that is close to the sensor array can be reconstructed. In addition, Fig. 1(f) shows the result using a 128-elements linear transducer, which is polluted by many artifacts.

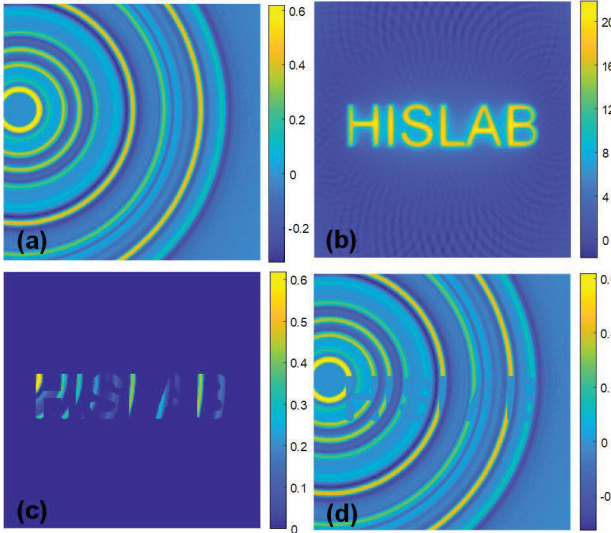


Fig. 2. Simulation results of DAS reconstruction. (a) The 5th-channel position-wise data. (b) The superposed results of 128-channel position-wise data. (c) d_{oj} of 5th-channel. (d) d_{ar} of 5th-channel.

Similarly, a more serious issue occurs in the result of DAS. In standard DAS, the received PA signals are simply delayed to every pixel based on the distance from detector to pixel's position as Fig. 2(a) shows, i.e., position-wise data. Since we cannot judge the accurate orientation of PA pressure, pixels of the same radius distance are usually arbitrarily assigned to the same value. We will obtain the reconstructed PA image if we superpose all channels' delayed data as Fig. 2(b) shows. We can divide the delayed data into the data of object d_{oj} and the data of artifact d_{ar} . Fig. 2(c) shows d_{oj} of 5th-channel delayed data, which is necessary for reconstruction. Fig. 2(d) shows d_{ar} of 5th-channel position-wise data, which is the components of the artifacts, although they are small and irrelevant for all channels. d_{ar} could cause severe interference when the system has sparse

number of detectors. Likewise, the DAS result fundamentally consists of p_{oj} and p_{ar} . Generally, d_{oj} and d_{ar} have similar scale, and p_{oj} usually has larger scale than p_{ar} . Considering same scale for position-wise data, it could be more equal to both objects and artifacts if we use position-wise data as the label to supervise model.

From above mentioned, the artifacts can be suppressed once we separate d_{oj} and d_{ar} . Some researches suppress the artifacts by limiting the effective angle between the signal delay direction and the detector or decreasing the sidelobe [6, 9, 32], which cannot solve this issue completely.

Moreover, the limited bandwidth of transducer induces some impacts for received PA signals, which usually cannot be changed after the system has been determined. Namely, the loss of signal is unavoidable in practical. Therefore, the focus of many researches is to minimize the loss algorithmically.

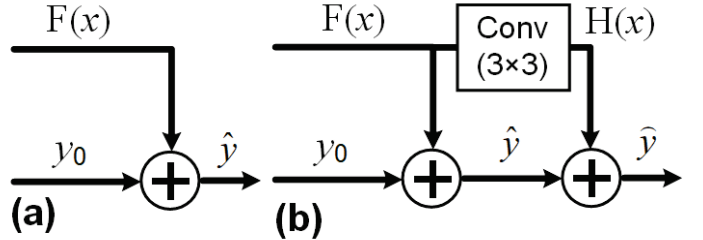


Fig. 3. The residual separation block. (a) Residual separation with single layer. (b) Residual separation with dual layers.

III. PROPOSED METHODS

A. Limited-view Compensation for PA Position-wise Data

To effectively resolve the limited-view problem, the plain method expects to train an end-to-end network by feeding a limited-view result. This scheme is regarded as image repair to learn the lost information from the data with the powerful deep learning approach, which could ignore the underlying physical meaning of each channel data. Inspired by [29, 30], for the first time to our best knowledge, we introduce a limited-view compensation for position-wise data, which simple delay the raw PA signals to every pixel. In this way, the location relation between each channel and the data of respective channel are treated as inputs of the CNN.

In our work, we demonstrate a quarter view data x with 32 channels as input of our model, which can be denoted by:

$$x = [d_1(h, w), d_2(h, w), \dots, d_{32}(h, w)]. \quad (5)$$

The output of model should generate another 96 channels' data by feeding x . We express this procedure as:

$$G(x) = [d_{33}(h, w), d_{34}(h, w), \dots, d_{128}(h, w)], \quad (6)$$

where $G(\cdot)$ denotes the DL model, and these 96 channels data are distributed covering the remaining 270° angles. Finally, we superpose these 128 channel data, i.e., $F(x) = \Sigma G(x) + \Sigma x$

(superpose along channel dimension), and obtain a full-view result of DAS.

B. Residual Separation Block

In previous works, most DL-based methods used limited-view PA image to train their end-to-end model, which crudely treats the input as an incomplete image. These model could not be sensitive to small values due to differences of scale in DAS result. However, the main structure of object can be boosted in DAS result since p_{obj} is common part for each channel. On the other hand, position-wise data distribute p_{obj} and p_{art} in every channel ($p_{\text{obj}} = \sum d_{\text{obj}}$, $p_{\text{art}} = \sum d_{\text{art}}$), which have similar scale. To decouple the tangle of reconstructed PA image, and maintain the strong constraint of object, we introduce the residual separation structure, which considers the characteristics of position-wise data and reconstructed result simultaneously.

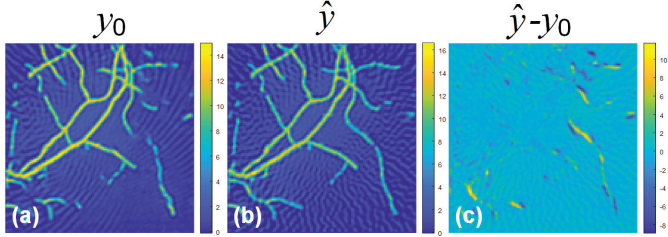


Fig. 4. The residual result, the average value of (c) is 0.062.

As shown in Fig. 3(a), we construct residual separation module with single layer, i.e., $\hat{y} = F(x) + y_0$. If we impose same desired label to y_0 and \hat{y} , $F(x)$ should asymptotically approximate to total zero even opposite y . Namely, the opposite y could be formatted if we choose an appropriate ground-truth for $G(x)$. Position-wise data are more focused on artifact than DAS result as we mentioned above (position-wise data are equal to artifact and object; DAS result is sensitive to object with large values), which may be a better choice to be the label of $G(x)$. In order to further constrain the approaching zero distribution of $F(x)$, we also set two additional losses, which will be described in next section. In Fig. 4, we show these three images in our results, and demonstrate the zero distribution in $F(x)$ as Fig. 4(c) shows. Therefore, we can train the proportion of respective branch to achieve the opposite object.

Furthermore, we recursively deepen residual module that $\hat{y} = H(x) + \hat{y}$ as Fig. 3 (b) shows, where $H(x) = W * F(x)$, and “ $*$ ” denotes convolution. We compare the performances with different layer in experiment.

C. Beyond Supervised Reconstruction Framework

As shown in Fig. 5, we introduce our proposed DL framework BSR-Net, which consists of two components. To fully leverage the benefit of complementary information from highly similar tasks, we proposed space-based calibration and removal module (SCRM) and two novel losses (response loss and overlay loss) to compensate the view in $G(x)$ and learn opposite information.

1) Space-based calibration and removal module

The above subnetwork generates 96-channel compensation data by feeding x , SCRM is used to replace the final layer of U-Net. We use SCRM to calibrate the angle from 90° to 270° , and remove the artifacts through the decoder. SCRM has been shown in Fig. 5, which connects the encoder features to the decoder.

For given feature map from encoder, we first conduct two transformations with max pooling and average pooling. These two feature maps are further fused with grouped fully-connected layer, intended to propagate information of corresponding position. If the input has m feature maps of size $n \times n$, the grouped fully-connected layer can decrease the number of parameters from mn^4 to $2mn^2$ compared to fully-connected layer. Finally, the feature map should be reshaped to $n \times n \times m$.

2) BSR-Net

We further introduce BSR-Net to integrate above methods. The overall architecture has been shown in Fig. 5, which can be divided two pipelines: position-wise data compensation and limited-view image inpainting.

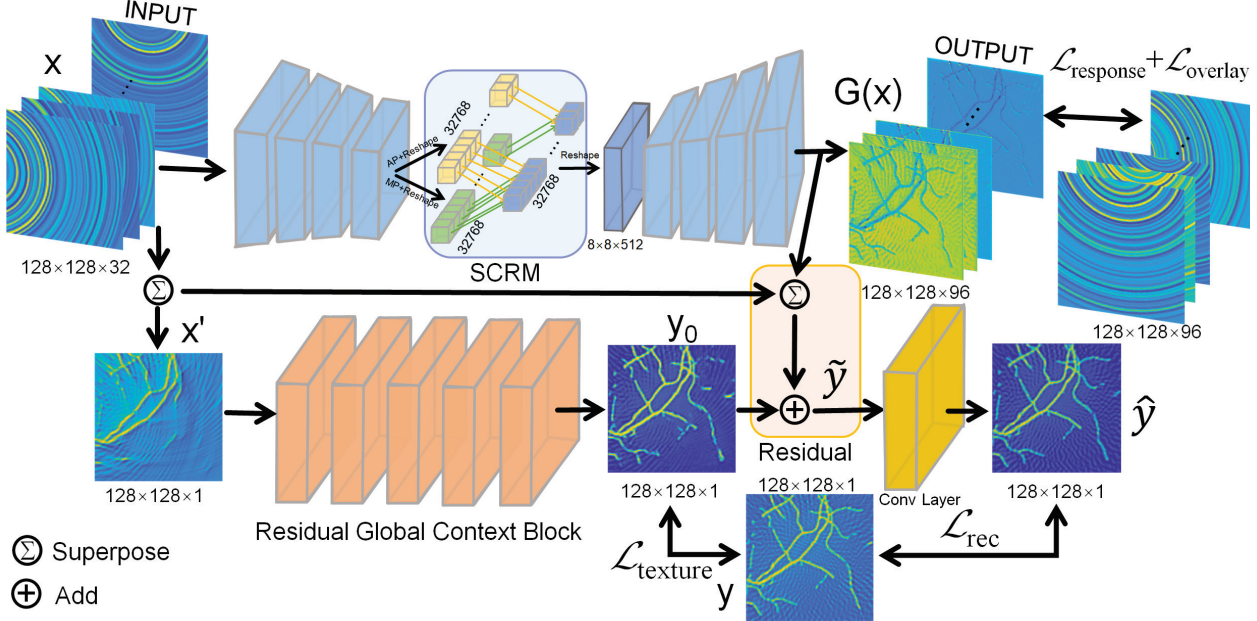
A U-Net [33] model is used for position-wise data compensation, which takes 32-channel position-wise data with a 90° limited view. Given an input data with size $128 \times 128 \times 32$, first four convolutional layers and the following pooling layer (fourth layer without pooling) are used to encode the position-wise data, followed final layer with a convolutional layer. SCRM can connect these feature maps to decoder with $8 \times 8 \times 128$ size. SCRM is followed by a series of five up-convolutional layers, and generates 96-channel position-wise data with other 270° view. For limited-view image inpainting, we use a small network to repair PA image, named Residual Global Context subnetwork (RGC-Net), which consists of five residual global context layers [34].

To fully leverage the benefit of complementary information from highly correlated data, we bridge these two results using residual separation. By combining response loss and overlay loss for $G(x)$, the artifacts in reconstructed result can be learned, which will be described in detail below.

3) Novel loss for beyond supervision

We train our BSR-Net by regressing to the ground truth content of full-view PA image. However, $F(x)$ has multiple equally plausible ways to satisfy the residual relation. We propose response loss and overlay loss to handle both the artifacts and the opposite object in the output.

The compensated delay data we expect to obtain is $G(x)$ in Eq. (6), which consists of additional N_l (96 in our paper) probe information. That means this layer l has N_l feature maps, each is with size M_l , where M_l (128×128 in our paper) is the height times the width of the feature map. Although all probes are spatially independently placed around the imaging target, their delayed data should have a dependent response relationship at the same position. Hence we built a response representation that computes the correlations between the different probe responses, where the expectation is taken over the spatial extend of the delay data. The responses between the two probes



are given by the Gram matrix [35] $G^l \in \mathcal{R}^{N_l \times N_l}$, where G_{ij}^l is the inner product between the vectorized delay data i and j in layer l :

$$G_{ij}^l = \sum_k F_{ik}^l F_{jk}^l. \quad (7)$$

The response loss is by minimizing the mean-squared distance between the entries of the Gram matrix from the original delay data and generated delay data (A^l and G^l denotes their respective response representations):

$$\mathcal{L}_{\text{response}} = \frac{1}{4N_l^2 M_l^2} \sum_{i,j} (G_{ij}^l - A_{ij}^l)^2. \quad (8)$$

Similarly, even though the resultant image is superimposed by the delayed data of all probes, the superposition of the two probes still has a certain dependence. Hence we built an overlay representation that computes the correlations between the different probe overlays. We propose an Overlay matrix $O^l \in \mathcal{R}^{N_l \times N_l \times M_l}$ to describe the overlays between vectorized delay data of the two probes n and n' :

$$O_{nn'm}^l = \sum_{n,n'} F_{nm}^l + F_{n'm}^l. \quad (9)$$

The overlay loss is by minimizing the mean-squared distance between the entries of the Overlay matrix from the original delay data and generated delay data (P^l and O^l denote their respective overlay representations):

$$\mathcal{L}_{\text{overlay}} = \frac{1}{4N_l^2 N_l^2 M_l^2} \sum_{n,n',m} (O_{nn'm}^l - P_{nn'm}^l)^2. \quad (10)$$

And then, we use a texture loss to supervise the limited-view image inpainting. We apply commonly-used mean square error (MSE) loss as our texture loss:

$$\mathcal{L}_{\text{texture}}(y_0) = \|y - y_0\|_F^2, \quad (11)$$

where F denotes the Frobenius norm. Furthermore, a reconstruction loss is used to optimize the residual result by minimizing the mean pixel-wise error:

$$\mathcal{L}_{\text{rec}}(\hat{y}) = \|y - \hat{y}\|_F^2. \quad (12)$$

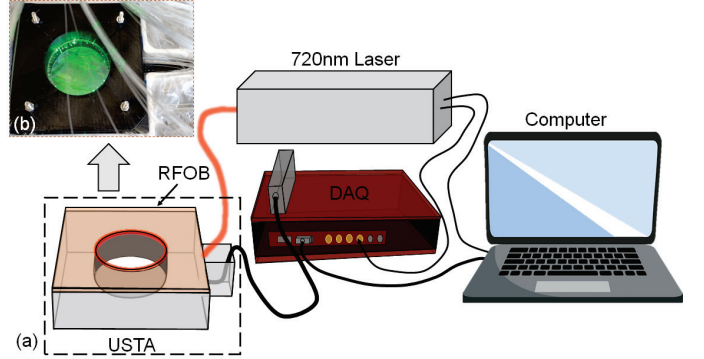


Fig. 6. (a) Schematics of the PACT system. (b) The detailed photograph of the black box region in (a). RFOB: ring-shaped fiber optics bundle; USTA: ultrasonic transducer array; DAQ: data acquisition system.

Finally, we define the overall loss function as follow:

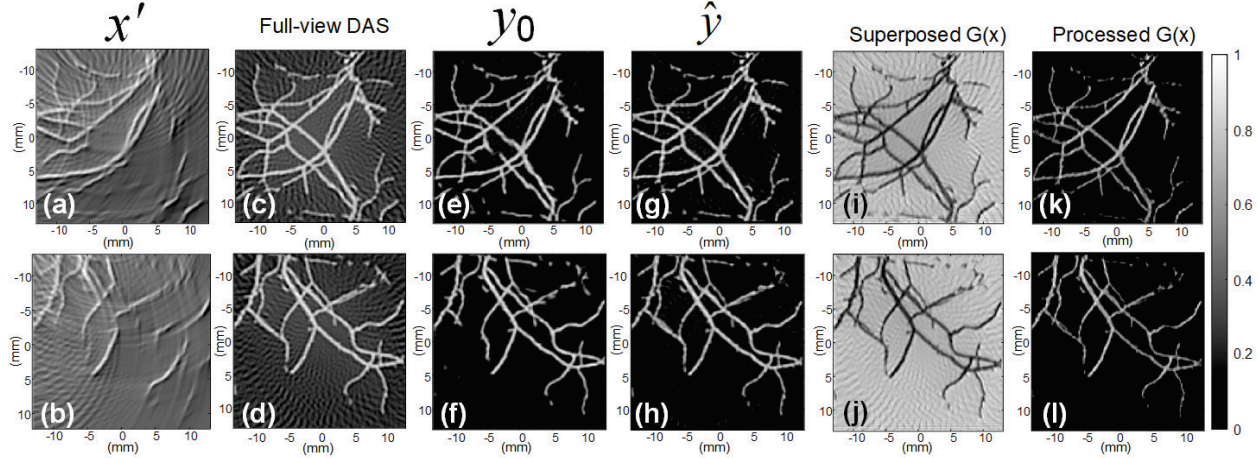


Fig. 7. Two examples of performance comparison of different results. (a,b) Limited-view DAS results. (c,d) Full-view DAS results. (e,f) y_0 results in BSR-Net. (g,h) \hat{y} results in BSR-Net. (i,j) $G(x)$ superposed along channel dimension in BSR-Net. (k,l) $G(x)$ superposed along channel dimension with the thresholding operation.

$$\begin{aligned} \mathcal{L}_{overall} = & \lambda_{re} \mathcal{L}_{response} + \lambda_{ov} \mathcal{L}_{overlay} \\ & + \lambda_{tex} \mathcal{L}_{texture} + \lambda_{rec} \mathcal{L}_{rec}, \end{aligned} \quad (13)$$

where λ_{re} , λ_{ov} , λ_{tex} , λ_{rec} are hyper-parameters that decide the proportion of every loss, which have different values in different experiments.

IV. EXPERIMENTS

In this section, we validate our method using both simulation and experimental data. All deep learning methods are implemented on Pytorch [36], which is an open-source framework. The high-speed graphics computing workstation is used to train our model, which consists of four NVIDIA RTX Titan graphics cards. All experiments are described in detail below. Furthermore, the source code is available at <https://github.com/chenyilan/BSR-Net>.

A. Training on Synthetic Vessels Data

We use the MATLAB toolbox k-Wave [37] to generate the synthetic dataset. The detectors surround the object evenly with 18 mm radius. The center frequency of all sensors is set as 2.5 MHz with 110% fractional bandwidth. The sound speed is 1480 m/s, and the reconstructed region is set as 26 mm \times 26 mm.

We use the public fundus oculi vessel DRIVE [38] as initial pressure distribution, which should be expanded by segmentation and combination to increase the data size. Finally, we have 2800 training sets and 200 test sets. In this experiment, we use 130, 0.02, 42, 60 for λ_{re} , λ_{ov} , λ_{tex} , λ_{rec} respectively.

B. Different Residual Layers Comparison

In order to compare the effect of different layers, we train another BSR-Net with two residual layers. Meanwhile, we compare plain method (0 residual layer), means y_0 in Fig.5, with 1 layer and 2 layers. This experiment is to validate that the residual structure can separate the object and the artifacts with the layer increasing deeper and deeper.

C. Ablation study for response and overlay loss

One of the contributions in this work is to propose two novel losses. To verify them, we compare the superposed $G(x)$ in four different cases as ablation study: remove these two losses, only use overlay loss, only use response loss and use these two losses. Therefore, the effect of these two losses could be validated in this experiment.

D. Training on Mice Data

Last but not least, we also verify the performance of our method on the data of mice abdomen. A customized PAT system (HisRing, HISLAB Inc., China) is employed to record PA signals as Fig. 6 shows, which is equipped with a 128-elements full-view ring-shaped transducer (2.5 MHz, Doppler Inc.). A pulsed laser (720nm wavelength, 10Hz repetition rate) is used to illuminate the object by a fiber optic bundle, which is evenly separated as a circle over the transducer as Fig. 6(b) shows, and the data sampling rate of our system is 40 MSa/s. The region of image reconstruction is 20mm \times 20mm.

We vertically scanned the mice using our system, and obtained 1100 training sets and 116 test sets, which are available at <https://ieee-dataport.org/documents/his-ring-abdomen>. In this experiment, we use 250, 0.6, 30, 40 for λ_{re} , λ_{ov} , λ_{tex} , λ_{rec} in Eq. (13), respectively.

V. RESULTS

A. Simulation results

We show two examples of imaging results from the test set in Fig. 7, which compares the limited-view results, full-view results, and three results in the procedure of BSR-Net. In addition, we simple process $G(x)$ and obtain the final result, which is called processed $G(x)$.

The obvious artifacts can be seen in full-view DAS from Fig. 7(c)-(d), which is the ground-truth of BSR-Net. The whole objects are recovered from the limited-view input comparing Fig. 7(e)-(f) with Fig. 7(a)-(b). Some of the details are distorted since RGC-Net is not deep enough. The vascular structure

becomes more complete after the addition of the two paths as Fig. 7(g)-(h) shows. In Fig. 7(i)-(j), the 96-channel data that should be position-wise data become the opposite object and artifacts with our novel supervision and residual structure. $G(x)$ should be further processed to separate objects and artifacts, and here we do simple threshold processing as Fig. 7(k)-(l) shows. In fact, the target could be separated better if we explore a more advanced processing method, which will be developed in the future work.

B. Evaluation of Different Residual Layers

One key component of our proposed method is the residual separation structure, which can be used repeatedly. In Fig. 5, we proposed BSR-Net with one-layer structure. In addition, we also compare BSR-Net with two-layers structure (Fig. 3(b)). Three different results indicate different structure as Fig. 8 shows. Fig. 8(a) indicates the output of RGC-Net, which is a plain solution for limited-view image calibration. Therefore, we call this procedure as 0 layer. The one-layer result has lower contrast and dynamic range ($[-60, 40]$) shown in Fig. 8(b), compared with two-layers result ($[-60, 200]$) shown in Fig. 8(c). However, the training of network will be increasingly difficult with the increase of the depth of residual structure.

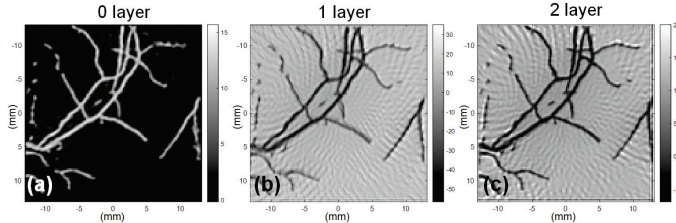


Fig. 8. Results of different residual layers. (a) The plain DL enhancement (none residual layer). (b) one residual layer. (c) 2 residual layers.

C. Ablation study results

The superposed $G(x)$ of four ablation studies have been shown in Fig. 9. $G(x)$ contains both objects and artifacts with small overall value if we do not supervise $G(x)$ as Fig. 9(a) shows, which can be regarded as a supplement to y_0 . $G(x)$ will be closer to y with only one loss shown in Fig. 9(b) and (c). These two losses are designed to focus on different characteristics of position-wise data (overlay loss focuses on the relation of each channel data; response loss focuses on the common area d_{oj} of each channel data). Therefore, the result of only using response loss has a higher contrast compared with that only using overlay loss. Obviously, the object and artifact can be separated into different ranges only when we use two losses simultaneously (negative objects and positive artifacts).

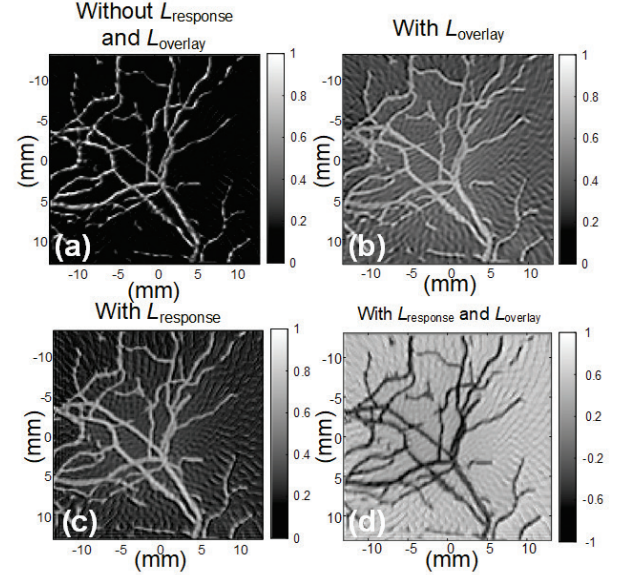


Fig. 9. The $G(x)$ results of ablation study for two novel losses. (a) The result without response loss and overlay loss. (b) The result with overlay loss. (c) The result with response loss. (d) The result with both response loss and overlay loss.

D. In-vivo results

Lastly, we demonstrated an *in-vivo* imaging result in Fig. 10, which is the abdomen of a mouse. We also show the limited-view result with 32 detectors, the full-view result with 128 detectors, three results of BSR-Net and the processed $G(x)$.

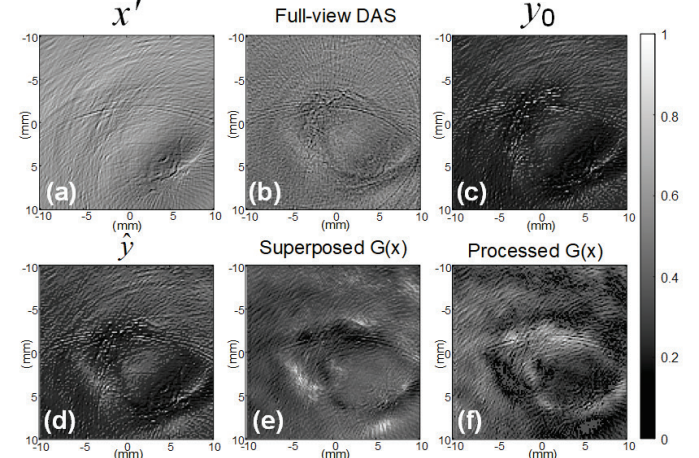


Fig. 10. The *in-vivo* results, (a) Limited-view DAS result. (b) Full-view DAS result. (c) y_0 result in BSR-Net. (d) \hat{y} result in BSR-Net. (e) $G(x)$ superposed along channel dimension in BSR-Net. (f) $G(x)$ superposed along channel dimension with thresholding operation.

Only a minor structure can be found in the limited-view result, and we even cannot recognize the outline of the object from Fig. 10(a). However, an explicit outline can be recognized from the full-view DAS result as Fig. 10(b) shows. All results from BSR-Net show higher contrast in Fig. 10(c)-(f). The complexity of the *in-vivo* experimental condition leads to the interference of imaging objects and artifacts compared with synthetic data before, which could cause a little difference between y_0 and \hat{y} as shown in Fig. 10(c) and (d). It is interesting that the artifacts

of $G(x)$ are relieved due to the residual structure in Fig. 10(e). Similarly, we further enhance Fig. 10(e) by threshold processing shown in Fig. 10(f), which clearly shows the profile of the mouse abdomen with a high contrast.

VI. CONCLUSION

The limited-view issue is inevitable in PACT system, which usually causes significant artifacts in the PA image. In this paper, we introduce a novel framework to solve the limited-view issue and the artifacts issue: limited position-wise data are used as input of deep learning model, and generate the position-wise data of lost view. A universal residual structure combined with a plain scheme is used to implement zero-distributive position-wise data. This method may inspire more research fields such as image de-noising, and foreground separation. Furthermore, we proposed two novel losses to constrain the position-wise output. Finally, we propose BSR-Net to implement the proposed framework. A quarter view data is fed into model, which outputs a group of full-view data. The numerical and *in-vivo* imaging results show that our methods have good performance to compensate the lost view and suppress artifacts. We have also published our data and codes to facilitate other researchers for further research. It is worth noting that $G(x)$ can be further used to extract more information, although we only use a threshold processing in this paper, which will be explored in the future work.

REFERENCES

- [1] L. V. Wang and S. Hu, "Photoacoustic tomography: *in vivo* imaging from organelles to organs," *Science*, vol. 335, no. 6075, pp. 1458-62, Mar 23 2012, doi: 10.1126/science.1216210.
- [2] Y. Zhou, J. Yao, and L. V. Wang, "Tutorial on photoacoustic tomography," *J Biomed Opt*, vol. 21, no. 6, p. 61007, Jun 2016, doi: 10.1117/JBO.21.6.061007.
- [3] L. V. Wang, "Tutorial on Photoacoustic Microscopy and Computed Tomography," *IEEE Journal of Selected Topics in Quantum Electronics*, vol. 14, no. 1, pp. 171-179, 2008, doi: 10.1109/jstqe.2007.913398.
- [4] D. Jiang, H. Lan, H. Zhong, Y. Zhao, H. Li, and F. Gao, "Low-Cost Photoacoustic Tomography System Based on Multi-Channel Delay-Line Module," *IEEE Transactions on Circuits and Systems II: Express Briefs*, vol. 66, no. 5, pp. 778-782, 2019, doi: 10.1109/tcsii.2019.2908432.
- [5] M. Xu and L. V. Wang, "Universal back-projection algorithm for photoacoustic computed tomography," *Phys Rev E Stat Nonlin Soft Matter Phys*, vol. 71, no. 1 Pt 2, p. 016706, Jan 2005, doi: 10.1103/PhysRevE.71.016706.
- [6] M. Mozaffarzadeh, A. Mahloojifar, M. Orooji, S. Adabi, and M. Nasirianyanki, "Double Stage Delay Multiply and Sum Beamforming Algorithm: Application to Linear-Array Photoacoustic Imaging," *IEEE Trans Biomed Eng*, Apr 05 2017, doi: 10.1109/TBME.2017.2690959.
- [7] A. A. Oraevsky, L. V. Wang, S. K. Kalva, and M. Pramanik, "Modified delay-and-sum reconstruction algorithm to improve tangential resolution in photoacoustic tomography," vol. 10064, p. 100643W, 2017, doi: 10.1117/12.2250487.
- [8] R. Paridar, M. Mozaffarzadeh, M. Mehrmohammadi, and M. Orooji, "Photoacoustic image formation based on sparse regularization of minimum variance beamformer," *Biomedical Optics Express*, vol. 9, no. 6, 2018, doi: 10.1364/boe.9.002544.
- [9] X. Ma, C. Peng, J. Yuan, Q. Cheng, G. Xu, X. Wang *et al.*, "Multiple Delay and Sum with Enveloping Beamforming Algorithm for Photoacoustic Imaging," *IEEE Transactions on Medical Imaging*, pp. 1-1, 2019, doi: 10.1109/tmi.2019.2958838.
- [10] C. Yang, H. Lan, F. Gao, and F. Gao, "Deep learning for photoacoustic imaging: a survey," *arXiv preprint arXiv:2008.04221*, 2020.
- [11] A. Hauptmann and B. Cox, "Deep Learning in Photoacoustic Tomography: Current approaches and future directions," *arXiv preprint arXiv:2009.07608*, 2020.
- [12] S. Guan, A. A. Khan, S. Sikdar, and P. V. Chitnis, "Fully Dense UNet for 2-D Sparse Photoacoustic Tomography Artifact Removal," *IEEE journal of biomedical and health informatics*, vol. 24, no. 2, pp. 568-576, 2019.
- [13] C. Yang and F. Gao, "EDA-Net: Dense Aggregation of Deep and Shallow Information Achieves Quantitative Photoacoustic Blood Oxygenation Imaging Deep in Human Breast," in *Medical Image Computing and Computer Assisted Intervention – MICCAI 2019*, (Lecture Notes in Computer Science, 2019, ch. Chapter 28, pp. 246-254).
- [14] C. Cai, K. Deng, C. Ma, and J. Luo, "End-to-end deep neural network for optical inversion in quantitative photoacoustic imaging," *Opt Lett*, vol. 43, no. 12, pp. 2752-2755, Jun 15 2018, doi: 10.1364/OL.43.002752.
- [15] N. Awasthi, R. Pardasani, S. K. Kalva, M. Pramanik, and P. K. Yalavarthy, "Sinogram super-resolution and denoising convolutional neural network (SRCN) for limited data photoacoustic tomography," *arXiv preprint arXiv:2001.06434*, 2020.
- [16] N. Awasthi, G. Jain, S. K. Kalva, M. Pramanik, and P. K. Yalavarthy, "Deep Neural Network Based Sinogram Super-resolution and Bandwidth Enhancement for Limited-data Photoacoustic Tomography," *IEEE Transactions on Ultrasonics, Ferroelectrics, and Frequency Control*, 2020.
- [17] T. Tong, W. Huang, K. Wang, Z. He, L. Yin, X. Yang *et al.*, "Domain Transform Network for Photoacoustic Tomography from Limited-view and Sparsely Sampled Data," *Photoacoustics*, p. 100190, 2020.
- [18] H. Lan, C. Yang, D. Jiang, and F. Gao, "Reconstruct the Photoacoustic Image Based On Deep Learning with Multi-frequency Ring-shape Transducer Array," in *2019 41st Annual International Conference of the IEEE Engineering in Medicine and Biology Society (EMBC)*, 2019: IEEE, pp. 7115-7118.
- [19] D. Allman, A. Reiter, and M. A. L. Bell, "Photoacoustic source detection and reflection artifact removal enabled by deep learning," *IEEE transactions on medical imaging*, vol. 37, no. 6, pp. 1464-1477, 2018.
- [20] S. Antholzer, M. Haltmeier, R. Nuster, and J. Schwab, "Photoacoustic image reconstruction via deep learning," in *Photons Plus Ultrasound: Imaging and Sensing 2018*, 2018, vol. 10494: International Society for Optics and Photonics, p. 104944U.
- [21] J. Schwab, S. Antholzer, R. Nuster, and M. Haltmeier, "Real-time photoacoustic projection imaging using deep learning," *arXiv preprint arXiv:1801.06693*, 2018.
- [22] N. Davoudi, X. L. Deán-Ben, and D. Razansky, "Deep learning optoacoustic tomography with sparse data," *Nature Machine Intelligence*, vol. 1, no. 10, pp. 453-460, 2019.
- [23] A. Hauptmann, F. Lucka, M. Betcke, N. Huynh, J. Adler, B. Cox *et al.*, "Model-Based Learning for Accelerated, Limited-View 3-D Photoacoustic Tomography," *IEEE Trans Med Imaging*, vol. 37, no. 6, pp. 1382-1393, Jun 2018, doi: 10.1109/TMI.2018.2820382.
- [24] Y. E. Boink, S. Manohar, and C. Brune, "A partially learned algorithm for joint photoacoustic reconstruction and segmentation," *arXiv preprint arXiv:1906.07499*, 2019.
- [25] C. Yang, H. Lan, and F. Gao, "Accelerated Photoacoustic Tomography Reconstruction via Recurrent Inference Machines," in *2019 41st Annual International Conference of the IEEE Engineering in Medicine and Biology Society (EMBC)*, 2019: IEEE, pp. 6371-6374.
- [26] Y. E. Boink, S. Manohar, and C. Brune, "A Partially-Learned Algorithm for Joint Photo-acoustic Reconstruction and Segmentation," *IEEE transactions on medical imaging*, vol. 39, no. 1, pp. 129-139, 2019.
- [27] H. Lan, K. Zhou, C. Yang, J. Cheng, J. Liu, S. Gao *et al.*, "Ki-GAN: Knowledge Infusion Generative Adversarial Network for Photoacoustic Image Reconstruction In Vivo," in *Medical Image Computing and Computer Assisted Intervention – MICCAI 2019*,

- (Lecture Notes in Computer Science, 2019, ch. Chapter 31, pp. 273-281.
- [28] H. Lan, D. Jiang, C. Yang, F. Gao, and F. Gao, "Y-Net: Hybrid deep learning image reconstruction for photoacoustic tomography in vivo," *Photoacoustics*, vol. 20, p. 100197, 2020.
- [29] S. Guan, A. A. Khan, S. Sikdar, and P. V. Chitnis, "Limited-View and Sparse photoacoustic tomography for neuroimaging with Deep Learning," *Scientific Reports*, vol. 10, no. 1, pp. 1-12, 2020.
- [30] M. W. Kim, G.-S. Jeng, I. Pelivanov, and M. O'Donnell, "Deep-learning Image Reconstruction for Real-time Photoacoustic System," *IEEE Transactions on Medical Imaging*, 2020.
- [31] C. Tian, M. Pei, K. Shen, S. Liu, Z. Hu, and T. Feng, "Impact of system factors on the performance of photoacoustic tomography scanners," *Physical Review Applied*, vol. 13, no. 1, p. 014001, 2020.
- [32] G. Matrone, A. S. Savoia, G. Caliano, and G. Magenes, "The delay multiply and sum beamforming algorithm in ultrasound B-mode medical imaging," *IEEE Trans Med Imaging*, vol. 34, no. 4, pp. 940-9, Apr 2015, doi: 10.1109/TMI.2014.2371235.
- [33] O. Ronneberger, P. Fischer, and T. Brox, "U-net: Convolutional networks for biomedical image segmentation," in *International Conference on Medical image computing and computer-assisted intervention*, 2015: Springer, pp. 234-241.
- [34] Y. Cao, J. Xu, S. Lin, F. Wei, and H. Hu, "Gcnet: Non-local networks meet squeeze-excitation networks and beyond," in *Proceedings of the IEEE International Conference on Computer Vision Workshops*, 2019, pp. 0-0.
- [35] L. A. Gatys, A. S. Ecker, and M. Bethge, "A neural algorithm of artistic style," *arXiv preprint arXiv:1508.06576*, 2015.
- [36] A. Paszke, S. Gross, F. Massa, A. Lerer, J. Bradbury, G. Chanan *et al.*, "Pytorch: An imperative style, high-performance deep learning library," in *Advances in neural information processing systems*, 2019, pp. 8026-8037.
- [37] B. E. Treeby and B. T. Cox, "k-Wave: MATLAB toolbox for the simulation and reconstruction of photoacoustic wave fields," *Journal of biomedical optics*, vol. 15, no. 2, pp. 021314-021314-12, 2010.
- [38] J. Staal, M. D. Abramoff, M. Niemeijer, M. A. Viergever, and B. van Ginneken, "Ridge-based vessel segmentation in color images of the retina," *IEEE Trans Med Imaging*, vol. 23, no. 4, pp. 501-9, Apr 2004, doi: 10.1109/TMI.2004.825627.